Creep properties of high dense $La_{9.33}Si_6O_{26}$ electrolyte for SOFCs

D.Ciria[a,b]**, M. Jiménez-Melendo[b]*, V. Aubin[c], G.Dezanneau[a]

[a] *Laboratoire Structures, Propriétés et Modélisation des Solides, UMR8580, CentraleSupelec, CNRS, Université Paris-Saclay, 3 Rue Joliot-Curie 91190 Gif Sur Yvette, France*

[b] *Departamento de Física de la Materia Condensada, Universidad de Sevilla, Aptdo. 1065, 41080 Sevilla, Spain*

[c] *Laboratoire Mécanique des Sols, Structures et Matériaux, UMR8579, CentraleSupelec, CNRS, Université Paris-Saclay, 3 Rue Joliot-Curie 91190 Gif Sur Yvette, France*

Abstract

High density $La_{9.33}Si_6O_{26}$ polycrystals were fabricated by conventional and spark plasma sintering starting from nanopowders synthesized by freeze-drying. The materials exhibit a homogeneous microstructure formed by equiaxed grains with average sizes of 1.1 μm and 0.2 μm-diameter depending on the sintering route. Compressive mechanical tests were performed in air at constant strain rate between 900 and 1300 °C. A gradual brittle-to-ductile transition was found with increasing temperature and/or decreasing strain rate. Grain boundary sliding is the main deformation mechanism in the ductile region, characterized by a stress exponent n = 1 for the conventional sintered (large-grained) material and n = 2 for the spark plasma sintered (fine-grained) material; in both cases, the activation energy for creep was 360 kJ/mol. Effective cation diffusivities have been derived from mechanical data by comparison with appropriate models. The creep properties of lanthanum silicates are reported here for the first time.

Keywords: Mechanical properties, Creep, Lanthanum Silicate, SOFC electrolyte, Grain boundary sliding

* Corresponding author:

Tel: +34 954 550938

E-mail: melendo@us.es

** Corresponding author:

Tel: +34 954 55 64 23

E-mail: dciria@us.es

1 Introduction

The high operating temperatures of Solid Oxide Fuel Cells (SOFCs) are responsible for high costs and the unsatisfactory durability and reliability of these devices [1, 2]. SOFC components are indeed subjected to harsh environments and severe thermo-mechanical stresses which induce progressive degradation of SOFCs in operation [3-5]. Currently, there is a growing research effort which aims at understanding the different degradation mechanisms affecting SOFCs [6]. At elevated temperatures, physical-chemical alterations [3-5, 7-9], thermo-elastic mismatches [10, 11], creep deformations [12] and uneven temperature distribution [13, 14] are undesirable phenomena which can take place in the system risking the mechanical integrity and the overall performance of the stack [10, 12, 13, 15].

An intense search is nowadays underway for SOFC materials with the objective of lowering the operating temperature and improving their operability [16-18]. In this context, lanthanum silicates are of great interest [19-22], exhibiting conductivities higher than those of the well-known oxide ionic conductor yttria-stabilised zirconia at intermediate temperatures [19, 22, 23]. Most of investigations on rare-earth silicates apatites have been devoted to characterizing and optimizing their microstructural and electro-chemical properties [21, 22, 24-28], since very few electrode materials were found to be compatible with such an electrolyte [29, 30]. However, the creep properties of these materials have not been investigated yet, despite their relevance in the material selection and design of devices.

The aim of the present work was thus to evaluate the influence of strain rate, stress, temperature and grain size on the high-temperature mechanical behaviour of lanthanum silicate (LSO) electrolytes fabricated by two different routes, conventional sintering (CS-LSO) and spark plasma sintering (SPS-LSO). The mechanical properties were evaluated by means of creep experiments performed in air at constant cross-head speed in the temperature range between 900 and 1300 °C. The experimental data were correlated with microstructural observations performed by scanning and transmission electron microscopy to identify the atomistic mechanisms of plastic deformation and the origin of failure in these materials at high temperatures. In this study, the importance of grain sliding in the deformation processes is underlined, which may help to define the range of temperatures at which stress relaxation might be more easily controlled in order to reduce the internal residual stresses. Additionally, the use of lanthanum silicate is currently hindered by the serious challenge that densification entails in the preparation of these materials [24, 25]. In this regard, this study has allowed to obtain valuable information on the transport processes of the slowest moving species in the oxyapatites, not known at present, which is essential for different mass transport-related processes, such as densification and grain growth. Therefore, the present data may help to devise optimum processing schedule, understand the state of stresses in SOFC components and improve the durability and reliability of these devices.

2 Experimental details

2.1 Sample preparation

$La_{9.33}Si_6O_{26}$ nanopowders were obtained by freeze-drying following the procedure described in Refs. [24] and [25]. Commercial precursor powders of lanthanum acetate sesquioxide $La(CH_3COO)_3 \cdot 1.5H_2O$ and TetraEthOxySilane (TEOS, $Si(OC_2H_5)$) were used as starting precursors. A mixture containing the commercial reagents, acetic acid and ultra-pure water was prepared. The resulting solution was sprayed into a liquid nitrogen bath to form frozen droplets, which were transferred into the freeze-dryer chamber, where the dehydration process was carried out under vacuum. The final product was an amorphous precursor which was further calcined in air at 1000 °C during 4 h. For conventional sintering, the nanopowder was shaped into pellets by uniaxial pre-pressing at 100 MPa followed by isostatic pressing at 750 MPa for 10 min, and then sintered in air at 1500 °C during 12 h. For spark-plasma sintering, the nanopowder was progressively heated in a graphite mold/die in a Dr. Sinter SPS furnace (Plateforme Frittage Flash, Thiais, France) up to 600 °C at a rate of 200 °C/min and then up to 1250 °C at 50 °C/min with a 5 min-soaking time, under a constant pressure of 100 MPa. The resulting pellets were finally submitted to a conventional thermal treatment at 800 °C in air for 24 h to burn all residual carbon species. The final density of the samples, determined using Archimedes' method, was 97.1% of the theoretical value of $La_{9.33}Si_6O_{26}$ (5300 kg/m^3) for CS-LSO and 99.6% for SPS-LSO. X-Ray diffraction analyses performed on both apatites confirmed the presence of the single $La_{9.33}Si_6O_{26}$ hexagonal phase (space group $P6_3/m$, PDF-2002 XRD pattern) with lattice parameters a = 9.724(5) Å and c = 7.186(4) Å, in agreement with previous results in $La_{9.33}Si_6O_{26}$ ceramics sintered at temperatures between 1500 and 1600°C [25, 31-33].

2.2 Mechanical characterization

Compressive deformation tests were performed on specimens of 5 x 3 x 3 mm^3 in size which were cut from the sintered pellets with a low-speed diamond saw. Mechanical tests were carried out at temperatures between 900 and 1300 °C (0.51 – 0.69 homologous temperature) in air at constant cross-head speeds between 5 and 50 µm/min (corresponding to initial strain rates $\dot{\varepsilon}_o$ of 1.7×10^{-5} and 1.7×10^{-4} s^{-1}, respectively). A universal machine with alumina rams was used to perform the tests, with a minimum detectable strain rate of 5×10^{-7} s^{-1} and an inaccuracy of ± 10%. Air atmosphere was chosen because a previous study on the mechanical response of these oxyapatites under different environments (air, argon and hydrogen) [34] showed the absence of mechanical/chemical changes. The specimens were sandwiched between pads of SiC to reduce as much as possible the friction with the alumina punching dies of the deformation machine. The recorded data, load versus time, were plotted as σ - ε curves, where σ is the true stress and ε is the true strain. Unless premature failure occurred, mechanical tests were discontinued after reaching a total true strain of 50% for subsequent microstructural observations. The mechanical data were analysed using the standard high-temperature power law for steady-state deformation [35] :

$$\dot{\varepsilon} = A\sigma^{n}d^{-p}\exp\left(-\frac{Q}{RT}\right) \quad (1)$$

where $\dot{\varepsilon}$ is the steady-state strain rate, A is a parameter depending on the deformation mechanism, d is the grain size, n is the stress exponent, p is the grain size exponent, Q is the activation energy for flow, R is the gas constant and T is the temperature.

Two independent methods were used to evaluate n and Q: (i) by comparing the flow stresses measured on different specimens deformed isothermally at various strain rates (n) or temperatures (Q) (conventional method); and (ii) by strain rates (n) or temperatures (Q) changes performed during a test on the same sample (differential method). In both cases, steady-state conditions have to be fulfilled in order to get meaningful values of the creep parameters.

2.3 Microstructural characterization

The microstructural characterization of as-prepared and deformed polycrystals was performed using a high-resolution FEI Teneo scanning electron microscope (SEM) and a FEI Talos transmission electron microscope (TEM) (Microscopy Service, CITIUS, University of Seville). To reveal grain boundaries, longitudinal sections were cut from the samples, mechanically polished and then thermally etched in air at 1200 °C for 3 hours. The relevant morphological parameters, grain size d, form factor F and orientation angle θ were measured from SEM micrographs using a semiautomatic image analyzer averaging over more than 500 grains on each material. The grain size has been taken as the equivalent planar diameter $d = (4(\text{grain area})/\pi)^{1/2}$; the form factor is a dimensionless parameter which gives quantitative information of the grain shape $F = 4\pi(\text{grain area})/(\text{grain perimeter})^2$, ranging from 0 for a segment to 1 for a circle; and the orientation angle θ is defined as the orientation of the largest diameter of the grain relative to a direction of reference. TEM samples were prepared following conventional techniques of mechanical grinding, dimpling and ion-milling of sliced sections.

3 Results and discussion

3.1 Microstructure of as-fabricated CS-LSO and SPS-LSO

Fig. 1 shows representative SEM micrographs of polished and thermally etched cross-sections of the as-fabricated materials. Both LSO-CS and LSO-SPS compounds exhibit a homogeneous microstructure formed by equiaxed grains with very little porosity, in agreement with density measurements. The grain size distributions in both materials are consistent with a lognormal law, as usually found in ceramic compounds, but with very different average grain sizes, d = 1.1 ± 0.6 μm in CS-LSO (**Fig. 2a**) and d = 0.2 ± 0.1 μm in SPS-LSO (**Fig. 2b**).

Regarding the form factor *F*, both materials show equiaxed grains with F = 0.8 ± 0.1 (**Fig. 2c**), indicating the absence of preferential directions.

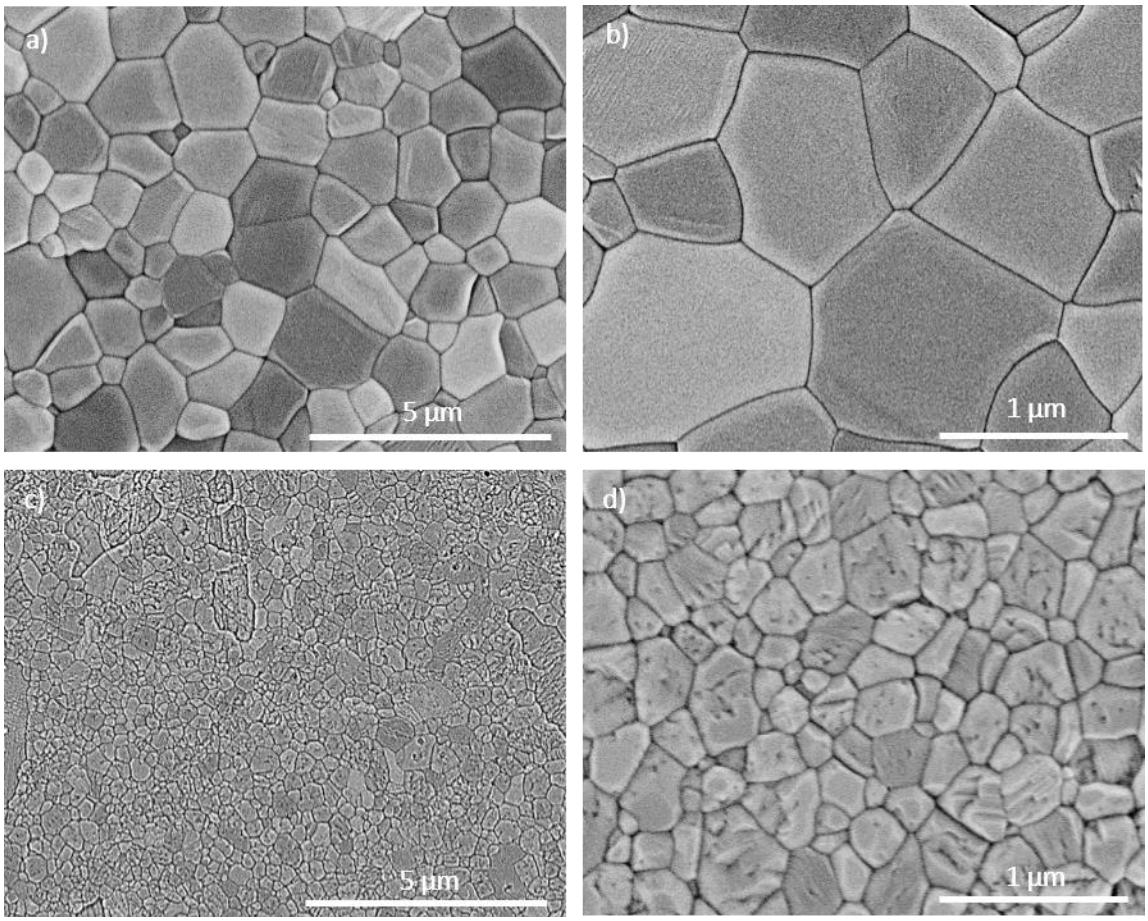

Fig. 1. SEM micrographs of as-prepared conventionally sintered (a,b) and spark plasma sintered (c,d) $La_{9.33}Si_6O_{26}$.

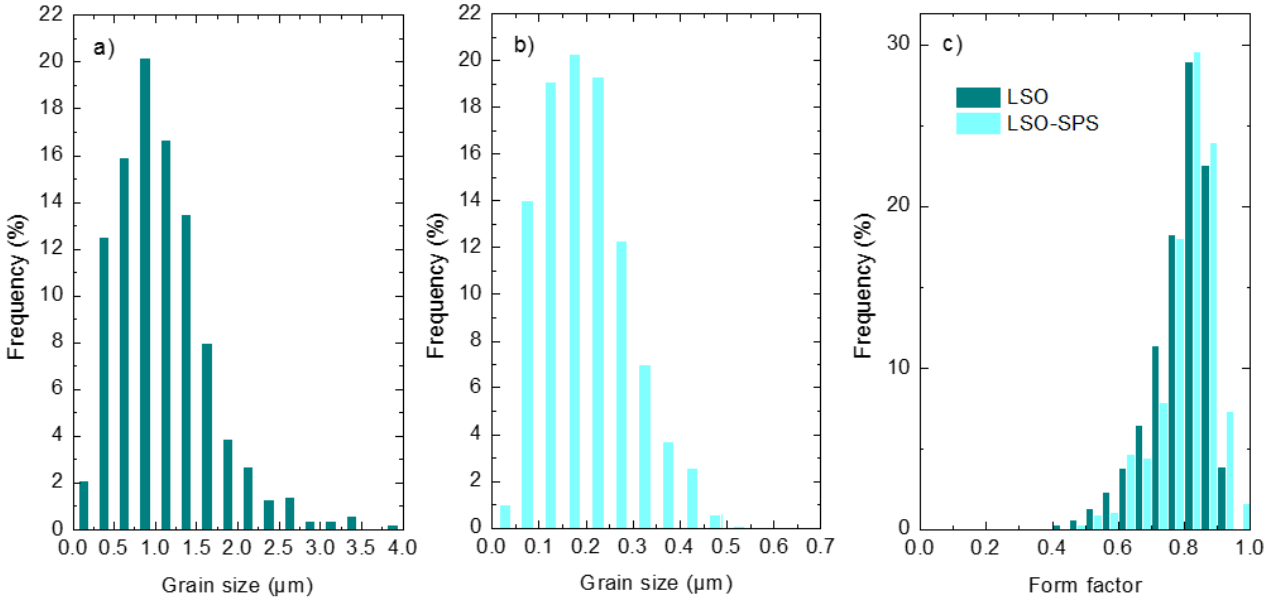

Fig. 2. Grain size distributions of (a) conventionally sintered and (b) spark plasma sintered $La_{9.33}Si_6O_{26}$. Note the different horizontal scale. (c) Form factor distributions of both materials.

The internal microstructure of the grains was investigated by TEM (**Fig. 3**). In both materials, the grains are free of dislocations and other defects, with clean and straight grain boundaries and well-defined triple points. No evidence of secondary phases along grain boundaries or in pockets was observed.

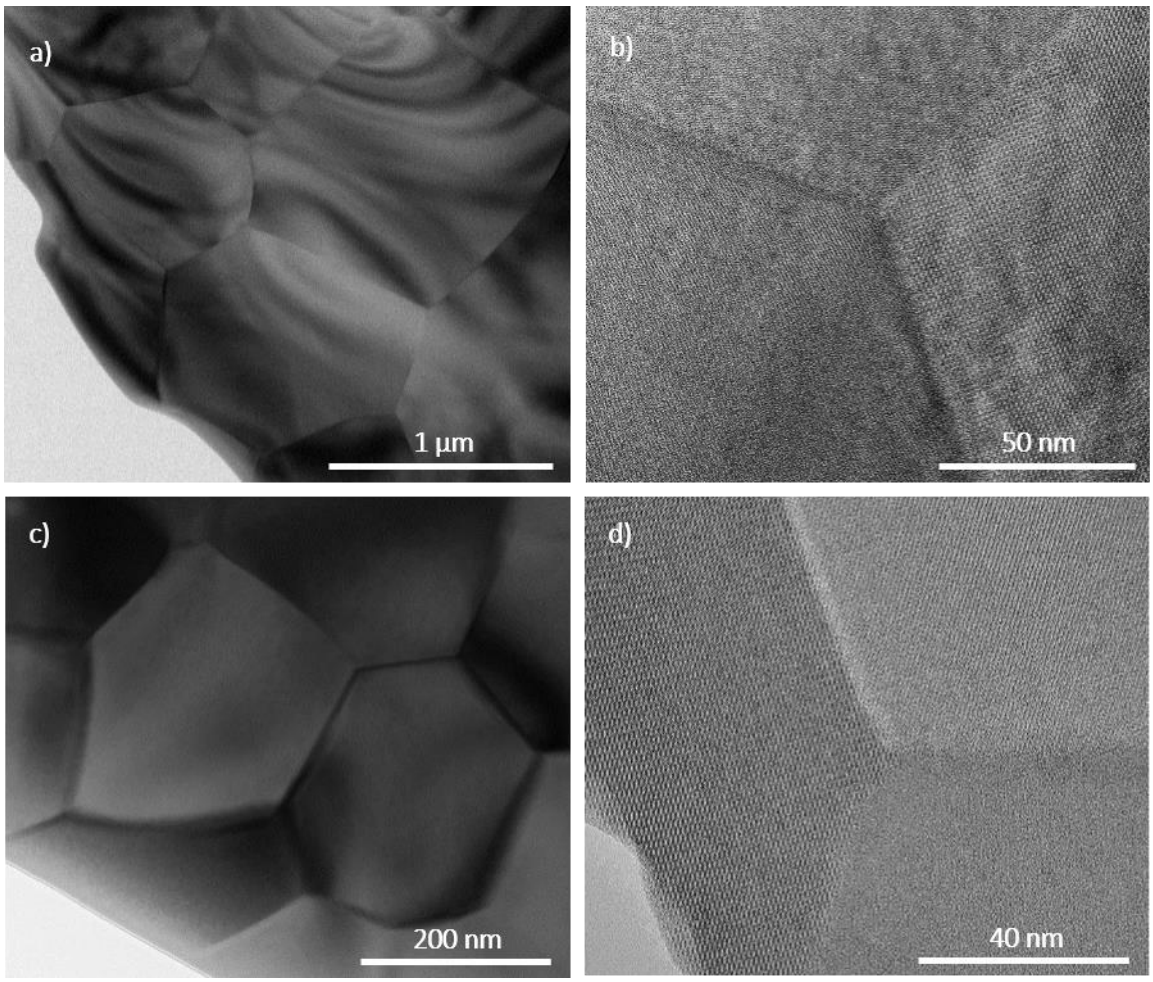

Fig. 3. TEM images of conventionally sintered (a,b) and spark plasma sintered (c,d) $La_{9.33}Si_6O_{26}$. Grains are free of defects, without secondary phases along grain boundaries and triple points.

3.2 High temperature mechanical behaviour

Fig. 4 shows typical curves of the variation of the true stress σ with true strain ε for different deformation conditions of temperature T and initial strain rate $\dot{\varepsilon}_o$ for CS-LSO apatites. The material displays a gradual transition from brittle-to-ductile regime as the temperature increases (**Fig. 4a**) and/or the strain rate decreases (**Fig. 4b**). At the lowest temperature studied, 1020 °C, the sample failed catastrophically at a stress level of 725 MPa without undergoing any plastic deformation. As the temperature increases, for a fixed initial strain rate, there is a progressive transition to a semibrittle behaviour, characterized by a negative slope of the σ - ε curve

(stress softening) due to material degradation. Such a behaviour is observed at 1140 °C and in the final part of the curve at 1200 °C (**Fig. 4a**). At both temperatures, however, the material reached deformations as large as 50% without macroscopic fracture. Finally, extended steady states of deformation (secondary creep regime) were attained at higher temperatures, characterized by a continuous increase in stress with strain due to the increase in specimen section and true strain rate during compression. A similar ductile-brittle transition was found when increasing the initial strain rate at a fixed temperature, as shown in **Fig. 4b**; flow softening can be observed at ε > 40% in the sample deformed at the highest strain rate.

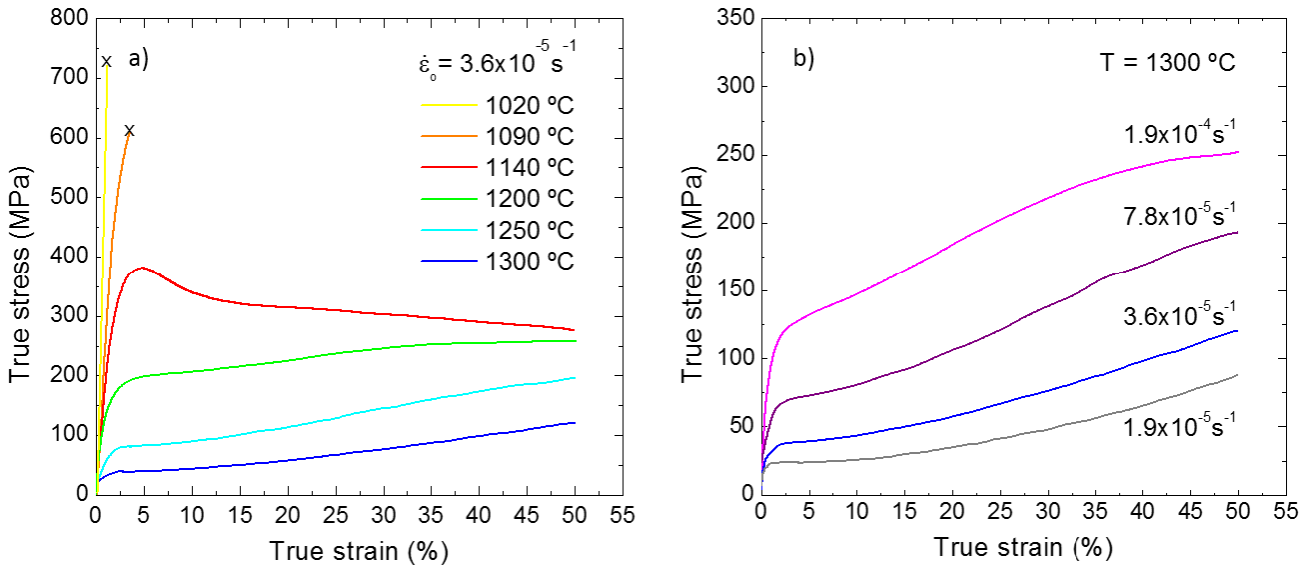

Fig. 4. True stress σ - true strain ε curves for CS-LSO deformed in compression: (a) at an initial strain rate of 3.6x10^{-5} s^{-1} as function of temperature; and (b) at 1300 °C as function of initial strain rate. Marks "x" indicate macroscopic specimen failure.

Fig. 5 shows representative σ - ε curves for SPS-LSO apatites obtained at different conditions of temperature and strain rate. The mechanical response of this material is qualitatively similar to that of CS-LSO, though shifted at temperatures about 200 °C below, owing to the difference in grain size. For a fixed initial strain rate of 3.6x10^{-5} s^{-1}, well-defined steady states of deformation were established at temperatures of 1020 °C and above. And for a fixed temperature of 1140 °C, secondary creep regimes were readily attained at all the strain rate studied. In such conditions, the slope of the σ - ε curves increases continuously with increasing $\dot{\varepsilon}_o$ (**Figs. 4b** and **5b**), as expected in constant cross-head speed tests.

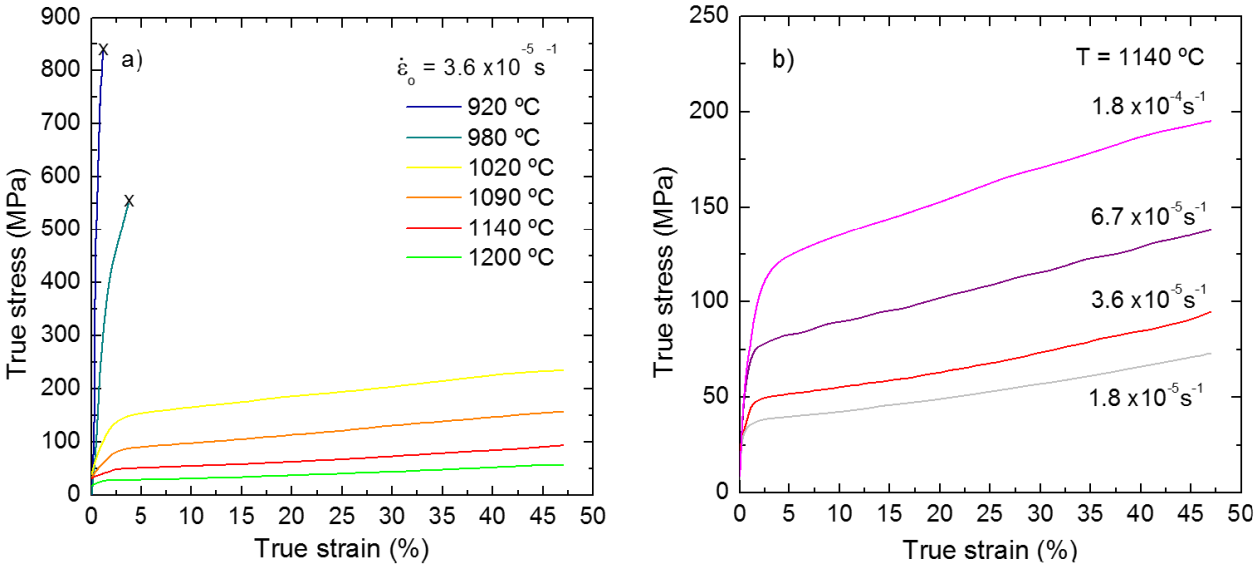

Fig. 5. True stress σ - true strain ε curves for SPS-LSO deformed in compression: (a) at an initial strain rate of $3.6x10^{-5}$ s^{-1} as function of temperature; and (b) at 1140 °C as function of initial strain rate. Marks "x" indicate macroscopic specimen failure.

The macroscopic aspect of the strained samples correlates well with the shape of the corresponding stress - strain curves. In the ductile region, the specimens deformed very homogeneously without signs of macroscopic damage. In such conditions, SEM observations in both materials (**Fig. 5a** and **c**) reveal that the grains retained their equiaxed shape, with a form factor essentially unaffected by the deformation process, with an average value of F = 0.80 ± 0.10. Some concurrent grain growth took place during testing at the highest temperatures studied, particularly in the finer-grained SPS-LSO material: final grain sizes of 0.4 ± 0.1 and 0.5 ± 0.2 µm were measured after 50% strain at 1140 and 1200 °C, respectively. Grain coarsening was minimal for CS-LSO; for instance, a final grain size d = 1.4 ± 0.5 µm was measured after 50% strain at the highest temperature and lowest strain rate studied.

In the semi-brittle regime, cracks parallel to the loading direction begin to develop on the specimens, resulting in the flow softening observed in the corresponding stress - strain curves. In such conditions, however, the material was able to tolerate the macroscopic flaws without cracking. These cracks eventually end up fracturing the sample at the worst testing conditions of strain rate and temperature. SEM observations of fracture surfaces in both materials have shown a mixed failure mode (**Fig. 6**), with preferential occurrence of transgranular fracture in the larger-grained regions.

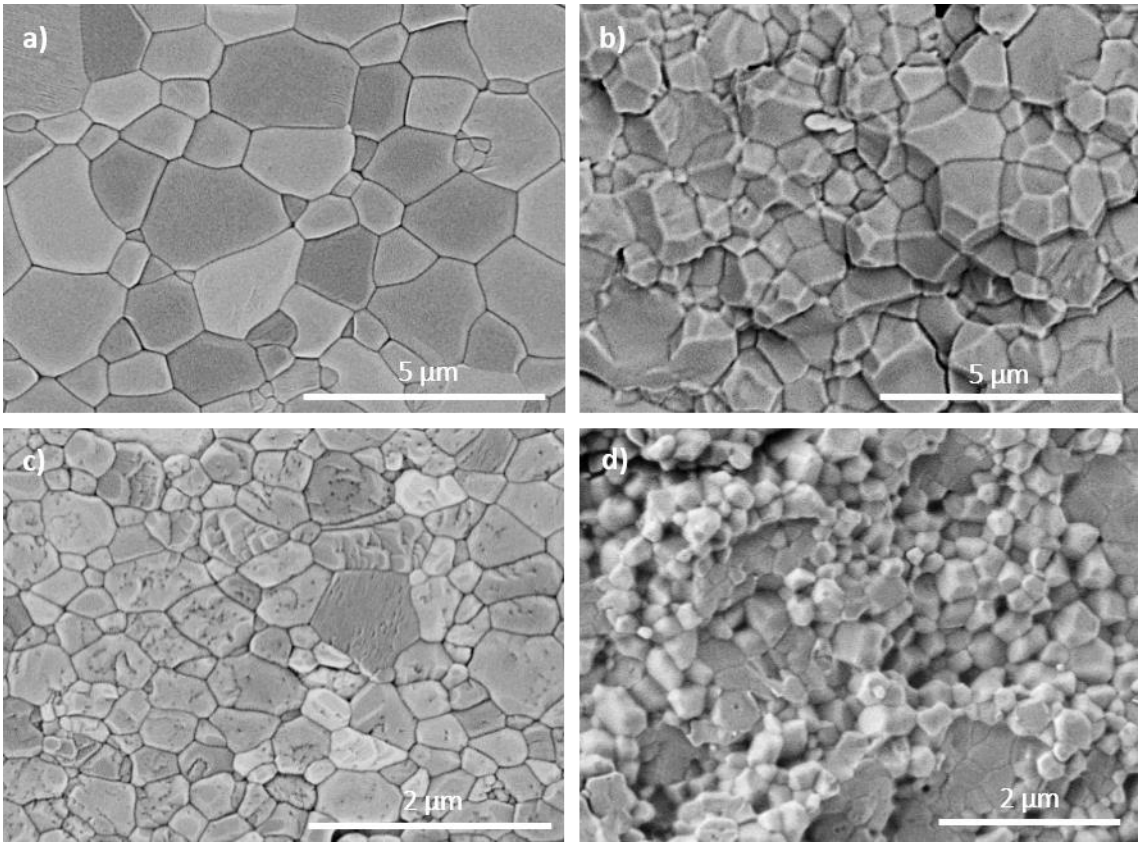

Fig. 6. SEM micrographs of (a,b) CS-LSO and (c,d) SPS-LSO samples deformed at an initial strain rate of 3.6×10^{-5} s^{-1} and different conditions of temperature: (a,c) in steady state up to $\varepsilon = 50\%$ at 1300 °C (CS-LSO) and 1090 °C (SPS-LSO); (b,d) fractured at 1090 °C (CS-LSO) and 920 °C (SPS-LSO). Stress axis vertical.

TEM observations of specimens deformed in the ductile regime (**Fig. 7**) have shown the absence of dislocations and other defects inside grains, which still exhibit straight boundaries and well-defined triple junctions after 50% strain, as in the as-fabricated materials. This result indicates that dislocations do not play any role in the high-temperature plastic deformation of both large and fine-grained oxyapatites.

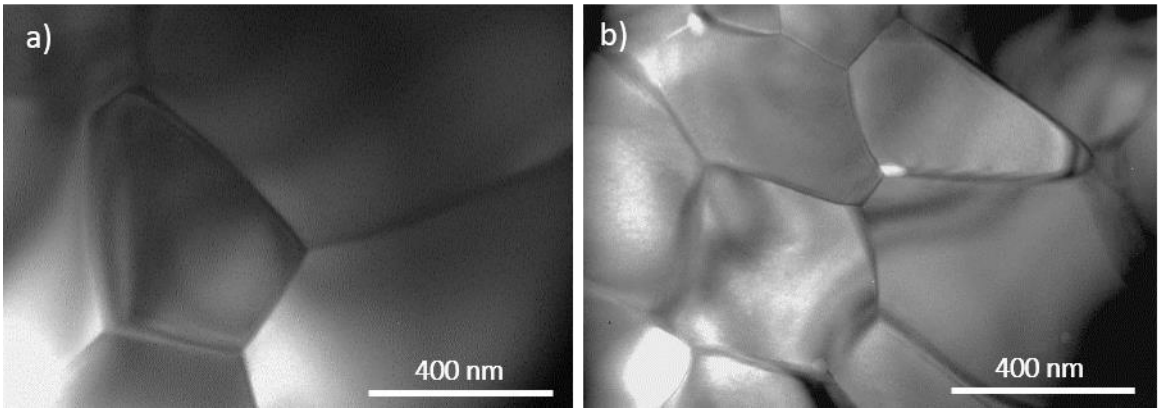

Fig. 7. TEM images of (a) CS-LSO and (b) SPS-LSO samples deformed in steady state at an initial strain rate of 3.6×10^{-5} s^{-1} and 1300 °C (CS-LSO) and 1140 °C (SPS-LSO).

3.3 Creep parameters

The stress exponent n and activation energy Q (Eq. (1)) were experimentally determined in the steady-state regime. The stress exponent n was estimated directly from the isothermal σ - ε curves obtained at different strain rates at a strain level of 10% (conventional method, **Fig. 8**), yielding average values of n = 1.1 ± 0.1 for CS-LSO and n = 2.0 ± 0.1 for SPS-LSO materials. The same n values were also estimated from fast strain rate changes during isothermal tests (differential method), as shown in **Fig. 9** for CS-LSO deformed at 1250 °C and for SPS-LSO deformed at 1075 °C, with strain rate changes between 3.6×10^{-5} and 1.8×10^{-5} s^{-1}. The comparison of the flow stresses before and after the strain rate changes yields average values of n = 1.1 ± 0.1 (8 determinations) and n = 1.9 ± 0.1 (10 determinations), respectively, in excellent agreement with the values deduced from conventional tests.

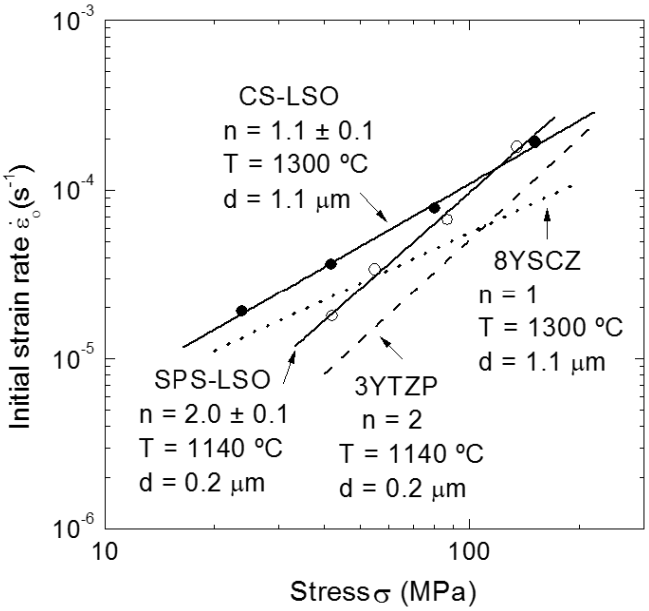

Fig. 8. Variation of strain rate with stress for CS-LSO at 1300 °C (closed symbols) and SPS-LSO at 1140 °C (open symbols), yielding stress exponents n of 1.1 ± 0.1 and 2.0 ± 0.1, respectively. Data for fine-grained 3YTZP with n = 2 [36], the reference material for superplastic ceramics, and for large-grained 8YSCZ with n = 1 [37] are also shown (dashed lines).

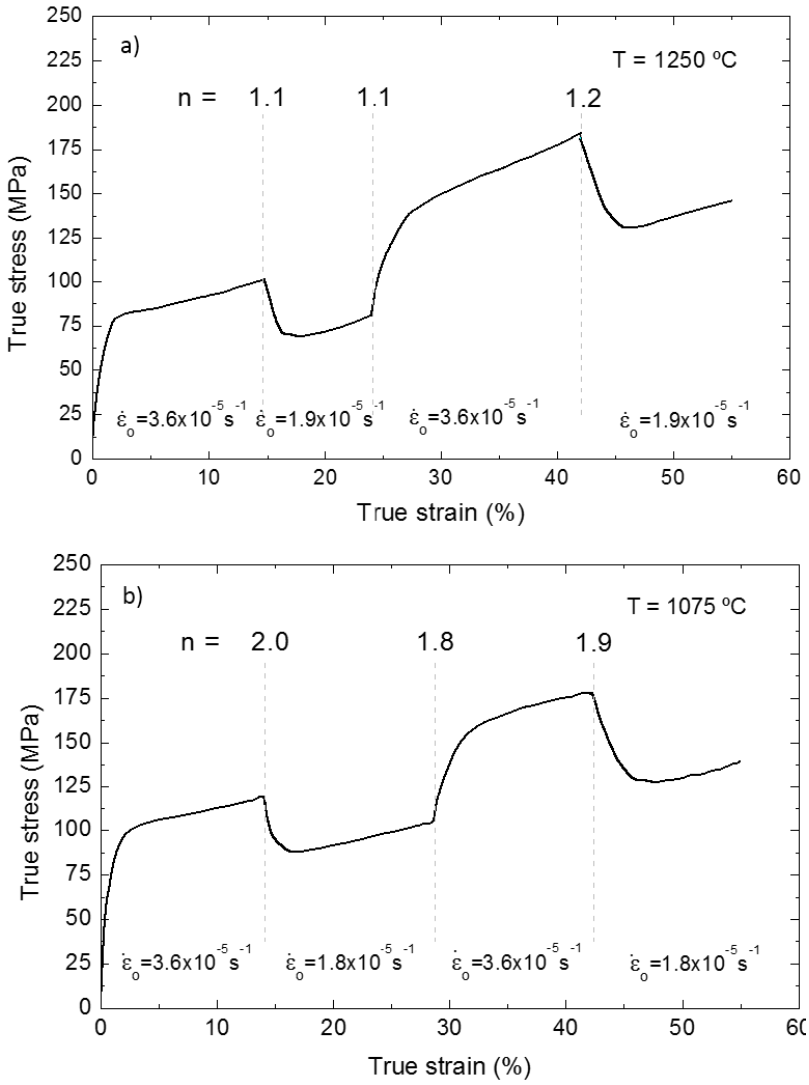

Fig. 9. True stress σ - true strain ε curves for (a) CS-LSO deformed at 1250 °C and (b) SPS-LSO deformed at 1075 °C, showing several strain rate changes to determine the stress exponent.

A stress exponent of 1 is characteristic of a diffusion-controlled grain boundary sliding mechanism, where the grains slide against each other to accommodate the macroscopic deformation of the specimen by mass transport without participation of dislocations [35, 38, 39]. The retention of the equiaxed grain shape after large strains (**Fig. 6a**) and the absence of dislocation activity (**Fig. 7a**) also support such a mechanism in conventionally sintered LSO. A stress exponent close to 1 has been reported previously in a large number of ceramic materials with grain sizes above 1 μm: NiO [40], UO_2 [41], cubic yttria-stabilized zirconia YSZ [42], yttrium aluminum garnet YAG [43], YBCO [44], $SrTiO_3$ [45], $La_{0.8}Sr_{0.2}Ga_{0.85}Mg_{0.15}O_3$ [46], $SrCo_{0.8}Fe_{0.2}O_3$ [47], $BaTiO_3$ [48] and $BaCe_{1-x}Y_xO_3$ (x = 0.05 - 0.20) [49].

On the other hand, a stress exponent n of 2 has been systematically reported in the superplastic behaviour of many metals and metallic alloys with d < 10 μm [39] as well as in submicrometer-grained ceramics (d < 1 μm), such as 3 mo% yttria-stabilized tetragonal zirconia 3YTZP [36], alumina [50], Al_2O_3/3YTZP composites [51], three-phase alumina/zirconia/mullite [52], and yttrium- and ytterbium-doped barium cerates [53, 54]. In these materials, it is well documented that grain boundary sliding also plays the key role in the deformation process,

without modifications of grain shape despite the very large strains attained, as found in the present work for the fine-grained SPS-LSO material.

For the sake of comparison, data for 8 mol% yttria-stabilized cubic zirconia 8YSCZ with n = 1 (extrapolated from 1400 °C [37]) and 3 mol% yttria-stabilized tetragonal zirconia with n = 2 [36] (the most widely studied superplastic ceramic) are also included in **Fig. 8** along with the data for the apatites. It can be seen that the creep strength of the oxyapatites is very similar to that of the corresponding zirconia with the same grain size, the difference being less than a factor of 2.

Following identical procedures, the creep activation energy Q was estimated from both the conventional and differential methods. In the former, Q was estimated from a plot of the flow stresses measured at 10% strain at different temperatures for a fixed initial strain rate (**Fig. 10**), yielding the same average value of Q = 360 ± 40 kJ/mol for both materials. This result suggests that the same diffusion mechanism, either into the lattice or along the grain boundaries, is the ultimate rate-controlling step in both large- and fine-grained oxyapatites, the deformation itself occurring by grain boundary sliding.

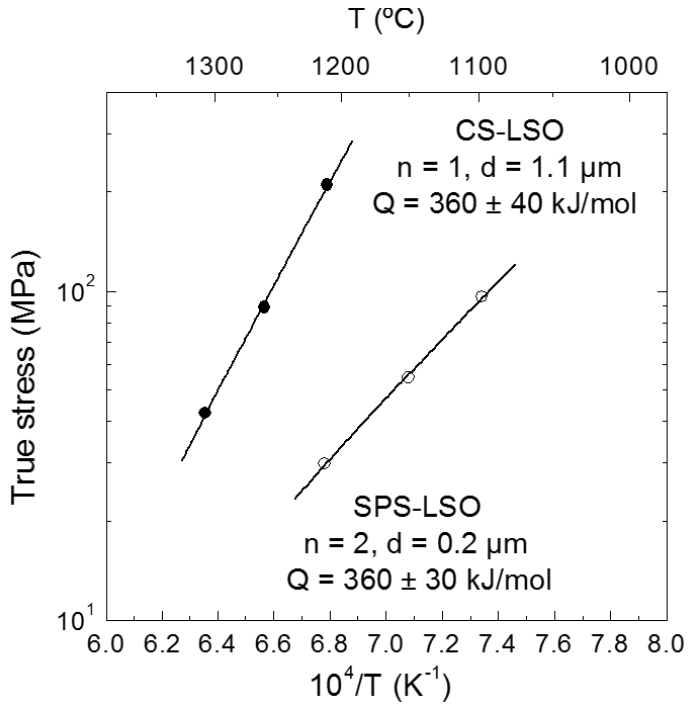

Fig. 10. Variation of flow stress with reciprocal temperature for CS-LSO (closed symbols) and SPS-LSO (open symbols) at an initial strain rate of 3.6×10^{-5} s^{-1}. Both sets of data lead to the same Q value (the difference in slopes is due to the different stress exponent).

The same Q value of 360 ± 40 kJ/mol has been measured by the differential method in CS-LSO (8 determinations) and SPS-LSO (8 determinations) materials, as shown in **Fig. 11**, where several determinations of Q by temperature changes at a fixed initial strain rate of 3.6×10^{-5} s^{-1} are displayed for CS-LSO and SPS-LSO. In both cases, the first temperature change led to energies of 360 and 365 kJ/mol, respectively, in excellent agreement with the Q values deduced previously from the σ - 1/T curves (**Fig. 10**). However, the second jump (between

1300 and 1250 °C for CS-LSO and between 1140 and 1050 °C for SPS-LSO) yielded higher Q values, particularly in the finer-grained material, indicating that the specimens became harder than expected because concurrent grain coarsening took place during the second sections of the differential curves carried out at higher temperatures, 1300 °C for CS-LSO and 1140 °C for SPS-LSO. It should be noted that, at difference with the stress exponent n determination where the strain rate changes are performed without unloading the sample, the deformation was stopped before each temperature change and then resumed after establishing the new thermodynamic equilibrium. The comparison with the isothermal tests performed at the same temperatures than the jumps (shown in **Fig. 11** for the different conditions of temperature) shows clearly such an effect of grain coarsening on flow stresses: while the stress levels in the first and second sections of the curves superimposed reasonably well, the third sections exhibit stresses higher than expected because of concurrent grain growth during deformation, as experimentally measured (see Section 3.2). Using Eq. (1), it can be easily calculated that an increase in grain size of 15-20% (depending on the value of the grain size exponent p in Eq. (1)) accounts for the difference in the values of Q for up- and down-temperature changes, the effect being much more pronounced for higher n values.

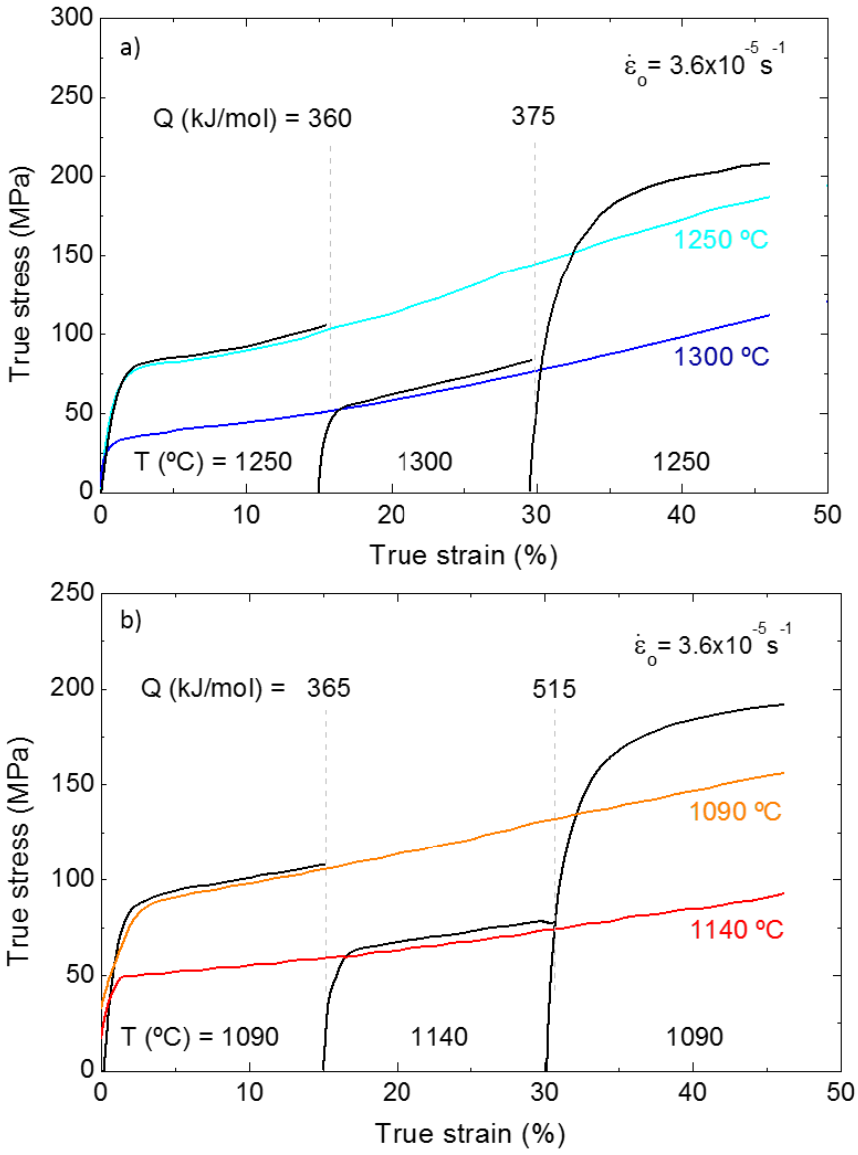

Fig. 11. True stress σ - true strain ε curves for (a) CS-LSO and (b) SPS-LSO deformed at an initial strain rate of 3.6x10^{-5} s^{-1} showing several determinations of Q by temperature changes. The corresponding conventional isothermal curves are also shown.

Fig. 11 also shows that steady states of deformation are readily obtained after each temperature change, indicating that the establishment or modification of a dislocation substructure is not necessary for attaining the stationary creep regime. This feature attests the previous idea that diffusion is the rate-controlling mechanism. The activation energy for flow Q = 360 kJ/mol = 3.7 eV can be thus associated with the activation energy for diffusion of the slowest moving species along the fastest path [40, 55]. In oxyapatite, the oxygen diffusion energy was reported to be of 0.7 eV in the (a, b) plane and 0.35 eV along the c-axis [56]. However, there is no information about cation diffusivities in LSO, although it is expected that cations are much slower than oxygen owing to the very high oxide ion conductivity of this material. The activation energy of 360 kJ/mol found in this

work is significantly higher than the oxygen diffusion energy and would thus mainly represent the activation energy for cation diffusion.

3.4 High-temperature deformation mechanisms in fine- and large-grained LSO apatites

In previous sections it has been shown that conventionally sintered apatites with d = 1.1 µm show a n value of 1 and a creep activation energy Q of 360 kJ/mol, while spark-plasma sintered apatites with d = 0.2 µm exhibit a stress exponent n of 2 and the same activation energy. In both materials, microstructural observations have shown the absence of dislocation activity as well as the lack of any modification in the shape of the grains with the deformation process. Taking all these results together, it can be concluded that diffusion-accommodated grain boundary sliding is the main deformation mechanism in both oxyapatites, the rate of deformation being controlled by the same diffusion process.

A value of n = 1 is typical of a Newtonian viscous creep behaviour, where the deformation rate is controlled by matter transport without dislocation activity [35, 39], the deformation being provided by mass transport itself (Nabarro-Herring and Coble models) or by grain boundary sliding (Asbby-Verrall model [38]). This last model has permitted to explain successfully the mechanical behaviour and microstructural features observed in different ceramic materials with grain sizes between 1 and 10 µm: UO_2, n = 1.5, d = 2-10 µm [41]; NiO, n = 1.4, d = 9 µm [40]; Y_2O_3-stabilized cubic ZrO_2, n = 1.3, d = 2-6 µm [42]; $YBa_2Cu_3O_{7-x}$, n = 1.0, d = 10 µm [44]; and yttrium aluminium garnet (YAG), n = 1.0, d = 2-5 µm [43]. In particular, this model accounts for the absence of changes in the form factor of the grains which retain their equiaxed shape even after very large strains and the absence of significant creep transients before the establishment of the steady-state regime, as found in the present materials. The steady-state strain rate in the Ashby-Verrall model is given by [38]:

$$\dot{\varepsilon} = \frac{98\sigma\Omega}{k_B T d^2}\left(D^{lat} + \frac{\pi\delta}{d}D^{gb}\right) \qquad (2)$$

where Ω is the molecular volume, k_B is the Boltzmann constant, δ is the grain boundary thickness and D^{lat} and D^{gb} are the diffusion coefficients for lattice and grain boundary diffusion, respectively. In compounds, D is an effective diffusion coefficient, usually referred as the "molecular" diffusion coefficient, which takes into account the diffusivities of the different species in the crystal along the various diffusion paths. To maintain the electrical neutrality of the crystal, D is usually controlled by the slower moving species along the fastest path [40, 55]. Because both diffusion processes, lattice and grain boundary, are independent and take place simultaneously, the total strain rate is the sum of the strain rates contributed by each process.

The increase in stress exponent from n = 1 to n = 2 when decreasing grain size below about 1 μm was firstly reported in yttria-stabilized zirconia polycrystals with grain sizes ranging from 0.3 to 17 μm [36]. There is currently no simple explanation for this effect, because the atomistic origin of the value n = 2 itself found in fine-grained superplastic materials is not clearly known and is still a matter of debate [36, 39, 55, 57, 58]. Many different models [39] have been developed to explain superplasticity, based in different relaxation processes of the stresses generated by the sliding of the grains on each other: dislocation motion, diffusional flow, interface-reaction-controlled diffusion, grain boundary migration, etc., none of them being able to explain successfully the body of experimental data in superplastic materials. The transition in n has been recently explained [58] in terms of a balance between the in-plane shear forces necessary for grain sliding and the local forces responsible for the accommodation process (grain reshaping). Most of the models predict a dependence of the steady-state plastic flow with the diffusion of the slowest moving ionic species either along grain boundaries or through the interior of the grains, usually associating p = 2 with $D = D^{lat}$ and p = 3 with $D = D^{gb}$ [35, 39].The change in stress exponent from 1 to 2 in the present materials has prevented the determination of p.

Unfortunately, there is no information available about cation diffusivities in oxyapatites, despite their importance in processes involving mass transport as creep, sintering and grain growth. Therefore, the validity of theoretical models for creep where diffusion is the ultimate strain rate-controlling step [35, 39]) cannot be directly checked by itself. An alternative approach has been then used in this study: the effective diffusivities in volume D^{lat} and along grain boundaries D^{gb} have been deduced and compared from individual creep data points by using appropriate deformation models with n =1 in the case of the large-grained apatite (Eq. 3) and with n = 2 for the fine-grained material. In this last case, due to the profusion of theoretical models and to avoid assuming any particular accommodation mechanism, the effective diffusivities have been derived from the phenomenological relationships developed by Sherby et al. [39] for superplastic metals corresponding to grain boundary sliding controlled by either lattice diffusion (n = 2, p = 2) or grain boundary diffusion (n = 2, p = 3):

$$\dot{\varepsilon} = 8x10^{6}\,\frac{Gb}{k_B T}\left(\frac{b}{d}\right)^{2}\left(\frac{\sigma}{G}\right)^{2} D^{lat}$$
$$\dot{\varepsilon} = 2x10^{5}\,\frac{Gb}{k_B T}\left(\frac{b}{d}\right)^{3}\left(\frac{\sigma}{G}\right)^{2} D^{gb} \qquad (3)$$

where b is the Burgers vector and G is the shear modulus. The first equation has been shown to account for the superplastic deformation of fine-grained yttria-stabilized tetragonal zirconia [36] and the second equation for fine fine-grained $YBa_2Cu_3O_{7-x}$ superconductor [59].

Fig. 12 shows the effective diffusivities D^{lat} and D^{gb} deduced from Eq. (2) for large-grained CS-LSO apatite and from Eq. (3) for fine-grained SPS-LSO apatite, assuming that the strain rate is controlled by either lattice or grain-boundary diffusion; a molecular volume $\Omega \simeq b^3$, with $b = 5$ Å, a grain boundary thickness $\delta = 1$ nm and a temperature-dependent shear modulus G measured by resonant ultrasound spectroscopy [34] have been used in the calculations. It can be seen that there is an excellent agreement between the grain boundary diffusivities deduced from the two independent steady-state creep rate equations, one with n = 1 in large-grained LSO and the other with n = 2 in fine-grained LSO. On the contrary, there is a difference of two orders of magnitude between the lattice diffusivities deduced from the two models. This agreement, with no adjustable parameters, lends credibility to the assumption that plastic flow is accommodated by grain boundary cation diffusion in lanthanum silicate oxyapatites, with an activation energy of 360 kJ/mol. To the best of our knowledge, it is the first time where such a comparison has been made in a material using two independent deformation models.

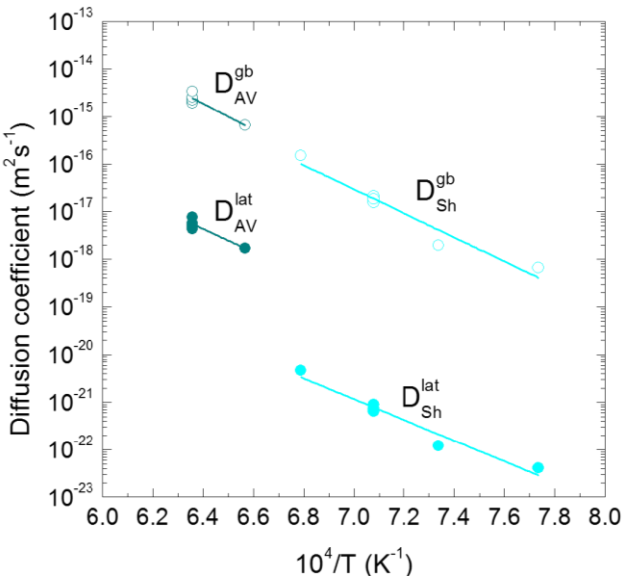

Fig. 12. Effective diffusivities in volume and along grain boundaries deduced from creep data in large-grained CS-LSO (AV, Eq. (2)) and in fine-grained SPS-LSO (Sh, (Eq. (3)). The agreement between the two independent models for grain boundary diffusion is remarkable.

4 Conclusion

High-density lanthanum silicate (LSO) ceramics with composition $La_{9.33}Si_6O_{26}$ were fabricated from nanocrystalline powders synthesized by freeze-drying by using two routes: conventionally sintering (CS) in air at 1500 °C for 12 h and spark plasma sintering (SPS) in air at 1250 °C for 5 min. The apatites exhibit homogeneous microstructures formed by equiaxed grains with average sizes of 1.1 µm and 0.2 µm for CS-LSO and SPS-LSO, respectively. High-temperature mechanical tests have been performed in air at constant initial strain rate be-

tween 900 and 1300 °C. A brittle-to-ductile transition was found with increasing temperature and/or decreasing strain rate in both materials, the transition temperature being about 200 ºC lower for SPS-LSO owing to the smaller grain size. In the ductile regime, the compounds exhibit extended steady states of deformation characterized by a stress exponent n of 1 for CS-LSO and 2 for SPS-LSO, both materials displaying the same creep activation energy of 360 kJ/mol. The values of n, along with the absence of dislocation activity and modifications in grain shape after strain, indicate that deformation is achieved primarily by grain boundary sliding. A comparison of the effective diffusivities derived from mechanical data by using appropriate independent deformation models with n = 1 and n = 2 suggests that grain boundary cation diffusion is the rate-controlling mechanism in oxyapatites regardless of grain size. When temperature decreases or strain rate increases, diffusion cannot longer accommodate the grain sliding, and cavitation takes place; in such conditions, however, the material is able to tolerate macroscopic cracks without fracture due to extensive grain boundary decohesion around the cracks. We report here for the first time the creep properties of lanthanum silicates.

5 Acknowledgment

This work was supported by the University Paris-Saclay (IDEX 2014); the Centre national de la recherche scientifique through the program “Instrumentation aux limites”; the University of Sevilla (VI PPIT-US); and the Spanish Ministerio de Ciencia, Innovación y Universidades (MAT2016-76526-R).

6 References

[1] S.P. Jiang, S.H. Chan, A review of anode materials development in solid oxide fuel cells, Journal of Materials Science 39(14) (2004) 4405-4439.
[2] E.D. Wachsman, K.T. Lee, Lowering the Temperature of Solid Oxide Fuel Cells, Science 334(6058) (2011) 935-939.
[3] Y.L. Liu, A. Hagen, R. Barfod, M. Chen, H.J. Wang, F.W. Poulsen, P.V. Hendriksen, Microstructural studies on degradation of interface between LSM–YSZ cathode and YSZ electrolyte in SOFCs, Solid State Ionics 180(23) (2009) 1298-1304.
[4] D. Simwonis, F. Tietz, D. Stöver, Nickel coarsening in annealed Ni/8YSZ anode substrates for solid oxide fuel cells, Solid State Ionics 132(3) (2000) 241-251.
[5] A. Nakajo, F. Mueller, J. Brouwer, J. Van herle, D. Favrat, Mechanical reliability and durability of SOFC stacks. Part I : Modelling of the effect of operating conditions and design alternatives on the reliability, International Journal of Hydrogen Energy 37(11) (2012) 9249-9268.
[6] J.I. Gazzarri, O. Kesler, Short-stack modeling of degradation in solid oxide fuel cells, Journal of Power Sources 176(1) (2008) 138-154.
[7] A. Hagen, R. Barfod, P.V. Hendriksen, Y.-L. Liu, S. Ramousse, Degradation of anode supported SOFCs as a function of temperature and current load, Journal of the Electrochemical Society 153(6) (2006) A1165-A1171.
[8] P. Tanasini, M. Cannarozzo, P. Costamagna, A. Faes, J. Van Herle, A. Hessler - Wyser, C. Comninellis, Experimental and theoretical investigation of degradation mechanisms by particle coarsening in SOFC electrodes, Fuel Cells 9(5) (2009) 740-752.
[9] Y.L. Liu, C. Jiao, Microstructure degradation of an anode/electrolyte interface in SOFC studied by transmission electron microscopy, Solid State Ionics 176(5) (2005) 435-442.
[10] A. Selçuk, A. Atkinson, Elastic properties of ceramic oxides used in solid oxide fuel cells (SOFC),

Journal of the European Ceramic Society 17(12) (1997) 1523-1532.
[11] T. Dey, D. Singdeo, M. Bose, R.N. Basu, P.C. Ghosh, Study of contact resistance at the electrode–interconnect interfaces in planar type Solid Oxide Fuel Cells, Journal of Power Sources 233 (2013) 290-298.
[12] A. Nakajo, J. Kuebler, A. Faes, U.F. Vogt, H.J. Schindler, L.-K. Chiang, S. Modena, J. Van herle, T. Hocker, Compilation of mechanical properties for the structural analysis of solid oxide fuel cell stacks. Constitutive materials of anode-supported cells, Ceramics International 38(5) (2012) 3907-3927.
[13] A. Nakajo, F. Mueller, J. Brouwer, J. Van herle, D. Favrat, Mechanical reliability and durability of SOFC stacks. Part II: Modelling of mechanical failures during ageing and cycling, International Journal of Hydrogen Energy 37(11) (2012) 9269-9286.
[14] E. Ivers-Tiffée, A. Weber, D. Herbstritt, Materials and technologies for SOFC-components, Journal of the European Ceramic Society 21(10) (2001) 1805-1811.
[15] L. Bouhala, S. Belouettar, A. Makradi, Y. Remond, Study of interface influence on crack growth: Application to Solid Oxide Fuel Cell like materials design, Materials & Design 31(3) (2010) 1033-1041.
[16] D.J.L. Brett, A. Atkinson, N.P. Brandon, S.J. Skinner, Intermediate temperature solid oxide fuel cells, Chemical Society Reviews 37(8) (2008) 1568-1578.
[17] T. Hibino, A. Hashimoto, T. Inoue, J.-i. Tokuno, S.-i. Yoshida, M. Sano, A low-operating-temperature solid oxide fuel cell in hydrocarbon-air mixtures, Science 288(5473) (2000) 2031-2033.
[18] B. Steele, Appraisal of Ce 1− y Gd y O 2− y/2 electrolytes for IT-SOFC operation at 500 C, Solid state ionics 129(1) (2000) 95-110.
[19] S. Nakayama, T. Kageyama, H. Aono, Y. Sadaoka, Ionic conductivity of lanthanoid silicates, Ln10(SiO4)6O3(Ln = La, Nd, Sm, Gd, Dy, Y, Ho, Er and Yb), Journal of Materials Chemistry 5(11) (1995) 1801-1805.
[20] S. Nakayama, M. Sakamoto, Electrical properties of new type high oxide ionic conductor RE10Si6O27 (RE = La, Pr, Nd, Sm, Gd, Dy), Journal of the European Ceramic Society 18(10) (1998) 1413-1418.
[21] S. Tao, J.T.S. Irvine, Preparation and characterisation of apatite-type lanthanum silicates by a sol-gel process, Materials Research Bulletin 36(7–8) (2001) 1245-1258.
[22] E.J. Abram, D.C. Sinclair, A.R. West, A novel enhancement of ionic conductivity in the cation-deficient apatite La9.33(SiO4)6O2, Journal of Materials Chemistry 11(8) (2001) 1978-1979.
[23] L. Leon-Reina, E.R. Losilla, M. Martinez-Lara, S. Bruque, M.A.G. Aranda, Interstitial oxygen conduction in lanthanum oxy-apatite electrolytes, Journal of Materials Chemistry 14(7) (2004) 1142-1149.
[24] A. Chesnaud, C. Bogicevic, F. Karolak, C. Estournes, G. Dezanneau, Preparation of transparent oxyapatite ceramics by combined use of freeze-drying and spark-plasma sintering, Chemical Communications (15) (2007) 1550-1552.
[25] A. Chesnaud, G. Dezanneau, C. Estournès, C. Bogicevic, F. Karolak, S. Geiger, G. Geneste, Influence of synthesis route and composition on electrical properties of La9.33 + xSi6O26 + 3x/2 oxy-apatite compounds, Solid State Ionics 179(33–34) (2008) 1929-1939.
[26] S. Célérier, C. Laberty, F. Ansart, P. Lenormand, P. Stevens, New chemical route based on sol–gel process for the synthesis of oxyapatite La9.33Si6O26, Ceramics International 32(3) (2006) 271-276.
[27] S. Celerier, C. Laberty-Robert, F. Ansart, C. Calmet, P. Stevens, Synthesis by sol–gel route of oxyapatite powders for dense ceramics: Applications as electrolytes for solid oxide fuel cells, Journal of the European Ceramic Society 25(12) (2005) 2665-2668.
[28] A. Vincent, S.B. Savignat, F. Gervais, Elaboration and ionic conduction of apatite-type lanthanum silicates doped with Ba, La10−xBax(SiO4)6O3−x/2 with x = 0.25–2, Journal of the European Ceramic Society 27(2–3) (2007) 1187-1192.

[29] M. Kahlaoui, A. Inoubli, S. Chefi, A. Madani, C. Chefi, Electrochemical and structural study of neodymium nickelate thick film deposited by spin coating on an oxyapatite electrolyte, Ionics 20(12) (2014) 1729-1735.
[30] X. Guo Cao, S. Jiang, Oxygen reduction reaction at (La,Sr) (Co,Fe)O3-δ electrode/La9.5Si6O26.25 apatite electrolyte interface of solid oxide fuel cells, International Journal of Hydrogen Energy 41 (2015).
[31] S. Lambert, A. Vincent, E. Bruneton, S. Beaudet-Savignat, F. Guillet, B. Minot, F. Bouree, Structural investigation of La9.33Si6O26- and La9AESi6O26+δ-doped apatites-type lanthanum silicate (AE=Ba, Sr and Ca) by neutron powder diffraction, Journal of Solid State Chemistry 179(8) (2006) 2602-2608.
[32] H. Okudera, Y. Masubuchi, S. Kikkawa, A. Yoshiasa, Structure of oxide ion-conducting lanthanum oxyapatite, La9.33(SiO4)6O2, Solid State Ionics 176(15–16) (2005) 1473-1478.
[33] J.E.H. Sansom, E. Kendrick, J.R. Tolchard, M.S. Islam, P.R. Slater, A comparison of the effect of rare earth vs Si site doping on the conductivities of apatite-type rare earth silicates, Journal of Solid State Electrochemistry 10(8) (2006) 562-568.
[34] D. Ciria, Thermomechanical properties of materials for fuel cells, Tesis, Univesity Paris-Saclay and University of Sevilla, 2017.
[35] J.-P. Poirier, Creep of Crystals: High-Temperature Deformation Processes in Metals, Ceramics and Minerals, Cambridge University Press, Cambridge, 1985.
[36] M. Jiménez-Melendo, A. Domínguez-Rodríguez, A. Bravo-León, Superplastic Flow of Fine-Grained Yttria-Stabilized Zirconia Polycrystals: Constitutive Equation and Deformation Mechanisms, Journal of the American Ceramic Society 81(11) (1998) 2761-2776.
[37] A.H. Chokshi, Diffusion, diffusion creep and grain growth characteristics of nanocrystalline and fine-grained monoclinic, tetragonal and cubic zirconia, Scripta Materialia 48(6) (2003) 791-796.
[38] M.F. Ashby, R.A. Verrall, Diffusion-accommodated flow and superplasticity, Acta Metallurgica 21(2) (1973) 149-163.
[39] T.G. Nieh, J. Wadsworth, O.D. Sherby, Superplasticity in Metals and Ceramics, Cambridge University Press, Cambridge, 1997.
[40] M. Jiménez-Melendo, A. Dominguez-Rodriguez, R. Marquez, J. Castaing, Diffusional and dislocation creep of NiO polycrystals, Philosophical Magazine A 56(6) (1987) 767-781.
[41] T.E. Chung, T.J. Davies, The low-stress creep of fine-grain uranium dioxide, Acta Metallurgica 27(4) (1979) 627-635.
[42] A. Bravo-León, M. Jiménez-Melendo, A. Domínguez-Rodríguez, Mechanical and microstructural aspects of the high temperature plastic deformation of yttria-stabilized zirconia polycrystals, Acta Metallurgica et Materialia 40(10) (1992) 2717-2726.
[43] M. Jiménez-Melendo, H. Haneda, H. Nozawa, Ytterbium Cation Diffusion in Yttrium Aluminum Garnet (YAG)—Implications for Creep Mechanisms, Journal of the American Ceramic Society 84(10) (2001) 2356-2360.
[44] M. Jiménez-Melendo, A.R. De Arellano-López, A. Domínguez-Rodríguez, K.C. Goretta, J.L. Routbort, Diffusion-controlled plastic deformation of YBa2Cu3Ox, Acta Metallurgica et Materialia 43(6) (1995) 2429-2434.
[45] D. Singh, M. Lorenzo-Martín, G. Chen, F. Gutiérrez-Mora, J.L. Routbort, High-temperature deformation behavior in SrTiO3 ceramics, Journal of the European Ceramic Society 27(11) (2007) 3377-3384.
[46] J. Wolfenstine, P. Huang, A. Petric, Creep behavior of doped lanthanum gallate versus cubic zirconia, Solid State Ionics 118(3) (1999) 257-259.
[47] G. Majkic, L. Wheeler, K. Salama, Creep of polycrystalline SrCo0.8Fe0.2O3−δ, Acta Materialia 48(8) (2000) 1907-1917.
[48] E.T. Park, P. Nash, J. Wolfenstine, K.C. Goretta, J.L. Routbort, High-temperature creep of

polycrystalline BaTiO3, Journal of Materials Research 14(2) (2011) 523-528.
[49] E.T. Park, K.C. Goretta, A.R. de Arellano-López, J. Guan, U. Balachandran, S.E. Dorris, J.L. Routbort, High-temperature deformation of BaCe1−xYxO3−y (0.05⩽x⩽0.2), Solid State Ionics 117(3) (1999) 323-330.
[50] F. Wakai, T. Nagano, T. Iga, Hardening in Creep of Alumina by Zirconium Segregation at the Grain Boundary, Journal of the American Ceramic Society 80(9) (1997) 2361-2366.
[51] F. Wakai, H. Kato, Superplasticity of TZP/Al 2 0 3 Composite, Adv. Ceram. Mat 3(1) (1988) 71-76.
[52] T. Chen, F.A. Mohamed, M.L. Mecartney, Threshold stress superplastic behavior and dislocation activity in a three-phase alumina–zirconia–mullite composite, Acta Materialia 54(17) (2006) 4415-4426.
[53] C. Vaquero-Aguilar, M.J. López-Robledo, J. Martínez-Fernández, C. Real, M. Jiménez-Melendo, High-temperature mechanical behavior of polycrystalline yttrium-doped barium cerate perovskite, Journal of the European Ceramic Society 31(7) (2011) 1333-1338.
[54] C. Vaquero-Aguilar, M. Jiménez-Melendo, Characterization and creep properties of proton-conducting Yb-doped barium cerate, Journal of the European Ceramic Society 31(14) (2011) 2671-2676.
[55] S. Swaroop, M. Kilo, C. Argirusis, G. Borchardt, A.H. Chokshi, Lattice and grain boundary diffusion of cations in 3YTZ analyzed using SIMS, Acta Materialia 53(19) (2005) 4975-4985.
[56] E. Béchade, O. Masson, T. Iwata, I. Julien, K. Fukuda, P. Thomas, E. Champion, Diffusion Path and Conduction Mechanism of Oxide Ions in Apatite-Type Lanthanum Silicates, Chemistry of Materials 21(12) (2009) 2508-2517.
[57] E. Alabort, P. Kontis, D. Barba, K. Dragnevski, R.C. Reed, On the mechanisms of superplasticity in Ti–6Al–4V, Acta Materialia 105 (2016) 449-463.
[58] C. Retamal, M. Lagos, B.M. Moshtaghioun, F.L. Cumbrera, A. Domínguez-Rodríguez, D. Gómez-García, A new approach to the grain-size dependent transition of stress exponents in yttria tetragonal zirconia polycrystals. The theoretical limit for superplasticity in ceramics, Ceramics International 42(4) (2016) 4918-4923.
[59] M. Jiménez-Melendo, A. Domínguez-Rodríguez, J.L. Routbort, Deformation maps of YBa2Cu3O7 − x superconductors, Scripta Metallurgica et Materialia 32(4) (1995) 621-626.